Pergamon

Geochimica et Cosmochimica Acta, Vol. 66, No. 23, pp. 4133–4148, 2002
Copyright © 2002 Elsevier Science Ltd
Printed in the USA. All rights reserved
0016-7037/02 $22.00 + .00

PII S0016-7037(02)00984-5

Consequences of diffuse and channelled porous melt migration on uranium series disequilibria

M. JULL,* P. B. KELEMEN,† and K. SIMS,‡

[1]Woods Hole Oceanographic Institute, Woods Hole, Massachusetts, 02543 USA

(*Received April* 29, 2001; *accepted in revised form May* 21, 2002)

Abstract—Magmas erupted at mid-ocean ridges (MORB) result from decompression melting of upwelling mantle. However, the mechanism of melt transport from the source region to the surface is poorly understood. It is debated whether melt is transported through melt-filled conduits or cracks on short time scales ($<\sim 10^3$ yrs), or whether there is a significant component of slow, equilibrium porous flow on much longer time scales ($>\sim 10^3$–10^4 yrs). Radiogenic excess ^{226}Ra in MORB indicates that melt is transported from the melting region on time scales less than the half life of ^{226}Ra (~1600 yrs), and has been used to argue for fast melt transport from the base of the melting column. However, excess ^{226}Ra can be generated at the bottom of the melt column, during the onset of melting, and at the top of the melt column by reactive porous flow. Determining the depth at which ^{226}Ra is generated is critical to interpreting the rate and mechanism of magma migration. A recent compilation of high quality U-series isotope data show that in many young basalts, ^{226}Ra excess in MORB is negatively correlated with ^{230}Th excess. The data suggest that ^{226}Ra excess is generated independently of ^{230}Th excess, and cannot be explained by "dynamic" or fractional melting, where observed radiogenic excesses are all generated at the base of the melt column. One explanation is that the negative correlation of activity ratios is a result of mixing of slow moving melt that has travelled through reactive, low-porosity pathways and relatively fast moving melt that has been transported in unreactive high-porosity channels. We investigate this possibility by calculating U-series disequilibria in a melting column in which high-porosity, unreactive channels form within a low-porosity matrix that is undergoing melting. The results show that the negative correlation of ^{226}Ra and ^{230}Th excesses observed in MORB can be produced if ~60% of the total melt flux travels through the low-porosity matrix. This melt maintains ^{226}Ra excesses via chromatographic fractionation of Ra and Th during equilibrium transport. Melt that travels through the unreactive, high-porosity channels is not able to maintain significant ^{226}Ra excesses because Ra and Th are not fractionated from each other during transport and the transport time for melt in the channels to reach the top of the melt column is longer than the time scale for ^{226}Ra excesses to decay. Mixing of melt from the high porosity channels with melt from the low-porosity matrix at the top of the melting column can produce a negative correlation of ^{226}Ra and ^{230}Th excesses with the slope and magnitude observed in MORB. This transport process can also account for other aspects of the geochemistry of MORB, such as correlations between La/Yb, $\alpha_{Sm/Nd}$, and Th/U and ^{226}Ra and ^{230}Th excess. *Copyright © 2002 Elsevier Science Ltd*

1. INTRODUCTION

Melt production beneath spreading ridges results from adiabatic decompression of upwelling mantle. As the mantle crosses its solidus and melts, the melt migrates upwards because it is less dense than the solid matrix. A fundamental question about this process is *How does melt accumulate and move to the surface?* Constraints from the composition of erupted magmas and physical models of melt transport have led to two end-member theories. One calls for fast, disequilibrium flow of melt through the mantle via melt-filled conduits or cracks (e.g., McKenzie, 1985, 2000). The other calls for a significant component of slower, equilibrium porous flow of melt, in which reaction forms high-porosity channels where melt is chemically isolated from the surrounding mantle (e.g., Spiegelman and Elliott, 1993; Kelemen et al., 1997; Lundstrom, 2000; Spiegelman et al., 2001). Note that this "disagreement" is somewhat artificial, because porous flow can lead to the formation of melt-filled conduits in some circumstances, and porous flow along grain boundaries is required to feed any type of conduit. However, implicit in the views of Spiegelman and Elliott (1993), Kelemen et al. (1997), Lundstrom (2000), and Spiegelman et al. (2001) is that a significant component of equilibrium diffuse porous flow occurs in the mantle, whereas in the view of McKenzie (1985, 2000), melt transport is near-fractional (i.e., "dynamic"), with melt being chemically isolated from the surrounding matrix as soon as a critical threshold porosity is reached.

Melt transport via melt-filled conduits relies on flow localization from "mechanical" instabilities that result from local variations in matrix strength, leading to the nucleation of melt filled fractures (Nicolas, 1989, 1990; Sleep, 1988; Connolly and Podladchikov, 1998; Suhr, 1999). Such features allow fast melt transport because melt velocities are limited only by Poiseuille flow. Melt transport via high-porosity channels relies on flow localization due to, for example, "reactive infiltration instabilities," whereby melt initially undergoing diffuse porous flow through a solid matrix with a solubility gradient organizes into distinct, high-porosity channels (Aharonov et al., 1995, 1997; Spiegelman et al., 2001). Porous flow localization might also be facilitated by mechanical instabilities (Stevenson, 1989;

* Author to whom correspondence should be addressed (jull@whoi.edu).
† pkelemen@whoi.edu
‡ ksims@whoi.edu

Kelemen and Dick, 1995; Hall and Parmentier, 1998; Richardson, 1998).

Direct observational evidence to constrain the mode of melt transport in the upper mantle beneath spreading ridges is provided by dunites exposed in ophiolite mantle sections and abyssal peridotites exposed at fracture zones near mid-ocean ridges. Here we use the term "dunite" to refer to rocks with more than 95% olivine, and the term "peridotite" to refer to rocks such as harzburgites and lherzolites with more than 40% olivine, less than 10% plagioclase, and pyroxene contents ranging from 5% to 50% or 60%. The dunites observed in Oman are compositionally distinct from the surrounding mantle and are interpreted as "replacive" features that have resulted from the localized dissolution of orthopyroxene and precipitation of olivine due to reactive porous flow of olivine saturated melt (Kelemen, 1990; Kelemen et al., 1995). It has been shown that these dunites are in chemical equilibrium with MORB, and that they are a likely pathway of focused porous flow in the mantle (Kelemen et al., 1995). In contrast, there is observational evidence from residual mantle peridotites and in ophiolites that the shallow mantle is not in major or trace-element equilibrium with MORB, indicating that there has not been chemical equilibration between aggregated MORB melts and shallow mantle at the top of the melting column (e.g., O'Hara, 1968; Johnson et al., 1990; Kelemen et al., 1995).

An important constraint on the mode of melt migration in the mantle comes from U-series disequilibria. Measurements of radiogenic excess ^{226}Ra and ^{230}Th in MORB reveal that these magmas are not in secular equilibrium (e.g., Reinitz and Turekian, 1989; Rubin and MacDougall, 1990; Volpe and Goldstein, 1993; Lundstrom et al., 1999; Sims et al., 2002). This observation has been used to place constraints on the physical processes and time scales associated with melting and melt migration in the mantle beneath spreading ridges (e.g., McKenzie, 1985; Spiegelman and Elliott, 1993; Lundstrom et al., 1995). However, debate exists on the interpretation of the U-series data. In particular, short-lived ^{226}Ra excess in MORB has been used to argue for both fast, disequilibrium melt transport from the base of the melting column (e.g., McKenzie, 1985, 2000), and slow, equilibrium melt transport extending to relatively shallow depths (e.g., Spiegelman and Elliott, 1993; Lundstrom et al., 1995).

Determining the depth at which ^{226}Ra is generated is critical to interpreting the rate and mechanism of magma migration. A recent compilation of high quality U-series isotope data show that in many young basalts, ^{226}Ra excess in MORB is negatively correlated with ^{230}Th excess (Sims et al., 2002). The data suggest that ^{226}Ra excess is generated independently of ^{230}Th excess, and cannot be explained by "dynamic" or fractional melting, where both ^{226}Ra and ^{230}Th excesses are generated at the base of the melt column. Lundstrom et al. (1995) suggested that the U-series data can be explained in terms of mixing of melts produced by deep and shallow melt columns that have different starting mineral modes. An alternative explanation, and one that we will test in this paper, is that the negative correlation of activity ratios represents a mixture of magmas, some of which have travelled through unreactive, high-porosity channels that form within a reactive, low-porosity matrix. In an effort to explain the U-series data, we investigate this possibility by calculating the U-series disequilibria and trace element chemistry within a self-consistent melt migration model.

2. U-SERIES DISEQUILIBRIA IN MORB

The state of equilibrium of parent-daughter isotopes in a radioactive decay series can be characterized in terms of an activity ratio, defined as $(\lambda_d c_d/\lambda_p c_p)$, where c is the concentration, λ is the decay constant (λ = ln(2)/half-life), and "*d*" and "*p*" subscripts refer to daughter and parent isotopes, respectively. Secular equilibrium for a parent-daughter isotope pair implies that the activity ratio is equal to one. In this state the production of daughter due to decay of the parent is exactly balanced by the decay of the daughter. If the activity ratio of a parent-daughter pair is not equal one, return to secular equilibrium will occur on a time scale proportional to the half-life of the daughter. For the ^{238}U decay chain $^{238}\text{U} \rightarrow ^{230}\text{Th} \rightarrow ^{226}\text{Ra}$, the half lives are $\sim 4.47 \times 10^9$, 7.52×10^4, and 1.60×10^3 yrs, respectively. Therefore in the convecting (subsolidus) mantle, which can essentially be treated as a closed system for the U-series isotopes, secular equilibrium is achieved for the ^{238}U decay series regardless of the source composition. The presence of disequilibria in U-series isotopes in MORB indicates that some process(es) disrupted the decay series on a time scale shorter than the half-life of ^{230}Th and ^{226}Ra.

Melting and transport of melt through the mantle can alter activity ratioes because different elements in a decay series have different solid/liquid partition coefficients. Consequently, the residence times of parent and daughter in the solid and liquid phase vary from element to element. If the daughter is more incompatible than the parent, "excess" concentrations of daughter in the melt will form. This is because the daughter is continuously produced in the solid at a rate faster than it can decay in the melt. Continued melting increases the concentration of the daughter in the melt. It has been argued that this process is responsible for ^{226}Ra and ^{230}Th excesses observed in MORB. In order to maintain the short-lived ^{226}Ra excess, rapid transport on the order of the half-life of ^{226}Ra ($\sim$1600 yrs) from the solidus to the surface is required (McKenzie, 1985, 2000).

However, reactive transport of melt in the mantle can change the relative concentrations of parent and daughter via chromatographic "fractionation". In a manner similar to melting, excess daughter can be generated if the daughter is more incompatible than the parent. This is because the daughter has a shorter residence time in the solid than the parent, and the parent continues to decay and generate excess daughter. Spiegelman and Elliott (1993) showed that if equilibration of melt with the solid mantle can occur as melt travels to the surface via equilibrium porous flow, chromatographic fractionation can produce ^{226}Ra excesses at shallow levels in the melting region, provided that porosities are sufficiently low ($\phi < D_{\text{parent}}$). This result relaxes the constraint on transport velocity because if radiogenic excesses are produced at the top of the melting column the melt has a shorter distance to travel in order to reach the surface.

Insight as to whether ^{226}Ra excess is a shallow or deep level signature of melt migration is possible from the systematics of ^{226}Ra and ^{230}Th excesses observed in MORB. Early measurements of U-series disequilibria suggested an inverse correlation

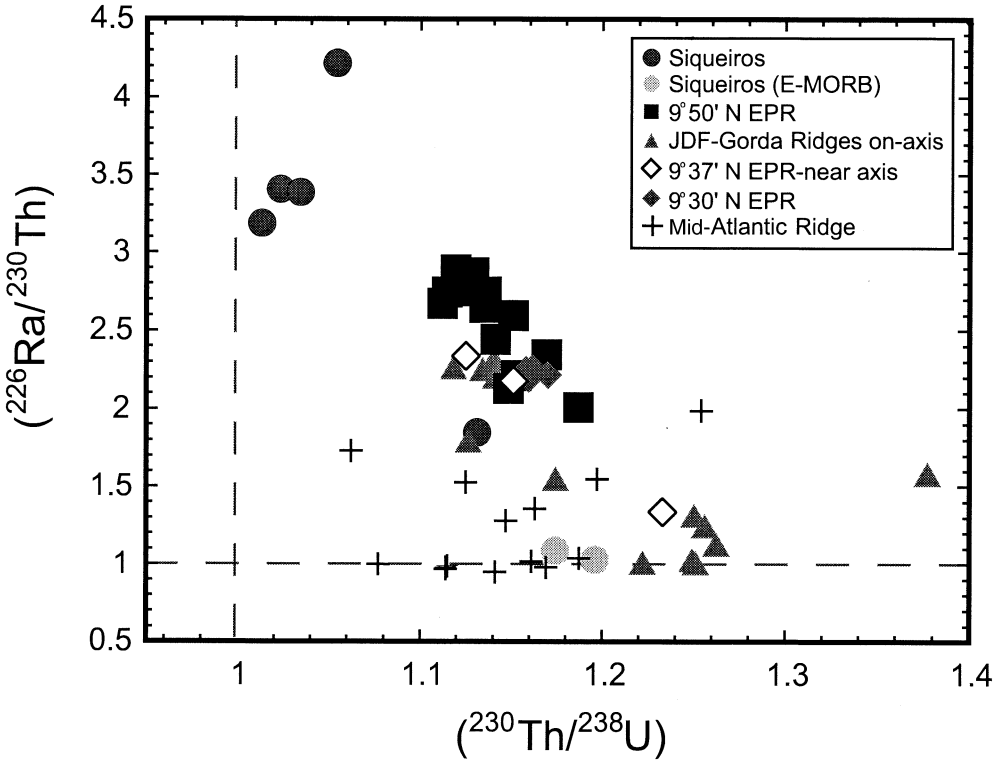

Fig. 1. Activity ratios measured in young MORB samples from the Siqueiros Fracture Zone, Juan de Fuca Ridge, East Pacific Rise (EPR), and the Mid-Atlantic Ridge. The negative correlation of the data is interpreted to represent primary melting processes (Sims et al., 2002). 9–10 °N EPR samples are from Sims et al. (2002); two EPR samples (replicated by Sims et al., 2002), are from Lundstrom et al., 1999; three "near-axis" EPR samples, including one E-type are from Batiza and Nu, 1992; Volpe and Goldstein, 1993; Juan De Fuca and Gorda ridge samples are from Volpe and Goldstein, 1993; Goldstein et al., 1989; Atlantic ridge samples are from Lundstrom et al., 1998; Siqueiros Transform samples from Lundstrom et al., 1999.

of ^{226}Ra and ^{230}Th excesses (Volpe and Goldstein, 1993) and this was interpreted to indicate that these excesses are generated independently from each other (Kelemen et al., 1997). If ^{226}Ra and ^{230}Th excesses observed in these lavas are both produced at the solidus, as suggested by McKenzie (1985), then a positive correlation should be observed because both excesses are produced at the solidus and radioactive decay during transport of this melt to the surface decreases the ^{226}Ra excess first, followed by the ^{230}Th excess on time scales comparable to the half-lives of these isotopes.

While data from the Juan de Fuca ridge (Lundstrom et al., 1995) and Siqueiros fracture zone (Lundstrom et al., 1999) have supported and strengthened the observed negative correlation between ^{226}Ra and ^{230}Th excesses first observed by Volpe and Goldstein (1993), interpretation of the MORB U-series data in terms of melting processes has been limited by large uncertainties in the sample eruption ages, magma storage times, and mantle source compositions. Most MORB suites measured for U-series disequilibria have been collected by dredging, which results in large uncertainties about the eruption age relative to the half-life of ^{226}Ra. Furthermore, very few of the MORB samples measured for U-series also have measurements of other radiogenic isotopes with long-lived parents (e.g., Nd, Sr, Pb, and Hf). In a new suite of analyses from young axial basalts (collected by Alvin) from the 9–10 °N East Pacific Rise, combined with a compilation of published analyses that are well constrained in terms of their age and source composition, Sims et al. (2002) show that the negative correlation of ^{226}Ra and ^{230}Th excess (Fig. 1) in these samples can be interpreted as a result of primary melting processes and not variation in source composition (i.e., variation in mineral mode). Importantly, the data compilation shows a negative correlation between ^{226}Ra and ^{230}Th over the entire data set, as well as within each individual suite of samples, supporting the conclusion that the correlation is not simply an artifact of local melting conditions or source composition. Furthermore, as a whole, the U-series data show well-defined correlations with incompatible element concentrations, with high ^{226}Ra excess lavas coinciding with lower [Ra], [Th], La/Yb, Na_8, and high Sm/Yb values. High ^{230}Th excess lavas coincide with high [Th], [U], La/Yb, Na_8, and lower Sm/Nd (see Figs. 9a–f of Sims et al., 2002).

3. DIFFUSE AND CHANNELLED POROUS MELT MIGRATION

A melt transport system in which porous flow produces ^{226}Ra excess at shallow levels while ^{230}Th excess is generated near the solidus is consistent with the observed negative correlation of ^{226}Ra and ^{230}Th excess (Kelemen et al., 1997). This requires that there be at least two distinct pathways for melt to travel through the melting column: one via low-porosity equi-

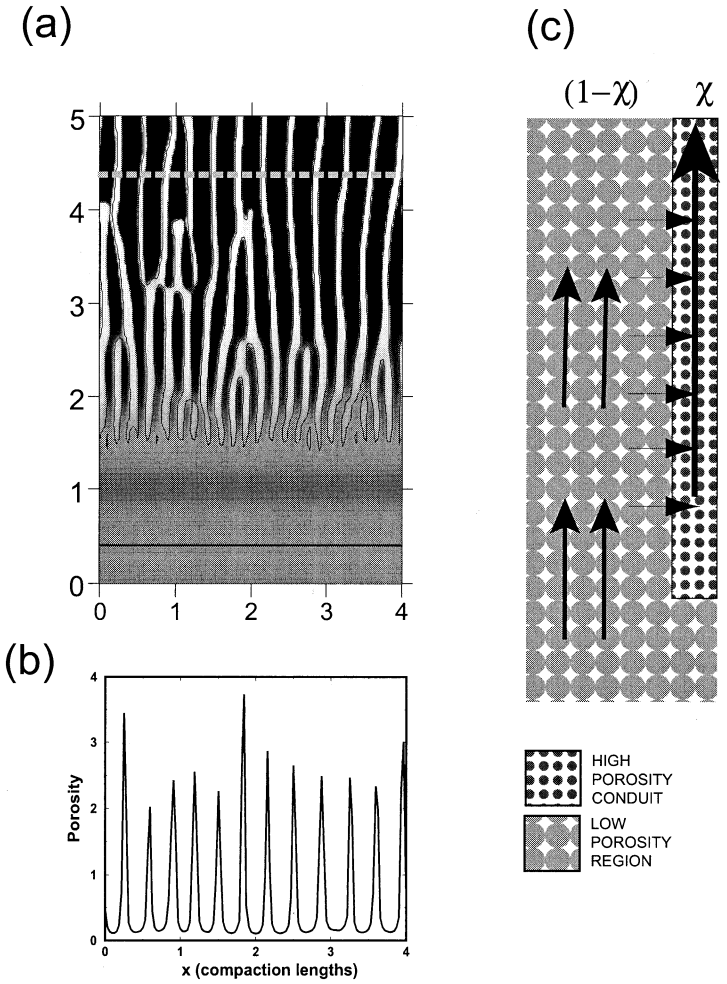

Fig. 2. (a) Calculated porosity distribution and (b) horizontal porosity profile resulting from a reactive infiltration instability, whereby fluid is allowed to flow through a porous and soluble solid. Direction of flow is from bottom to top. High-porosity channels are shown with interchannel regions of low porosity (from Spiegelman et al., (2000). The porosity profile in (b) is taken from along the dashed line shown in (a). (c) Simplified transport model used to assess the consequence of the flow organization shown in (a). At a given height in the model, high-porosity channels can form and melt is transferred to these channels as the solid matrix upwells and melts. The scaling term χ allows the porosity to be adjusted according to the horizontal extent of the high- and low-porosity regions.

librium porous flow, and the other via high-porosity channels. Spiegelman et al. (2001) have shown that if melt transport occurs via reactive porous flow, then high-porosity channels form in a background low-porosity matrix as a result of a reactive infiltration instability (Fig. 2a). causing a bi-modal distribution of porosity (Fig. 2b) From the single melt column models of Spiegelman and Elliott (1993) it is not clear whether production of shallow-level ^{226}Ra excess and near-solidus generation of ^{230}Th excess is possible within a melt migration model such as that shown in Figure 2. Though Iwamori (1994) and Lundstrom (2000) considered the effect of a "two-porosity" melt transport regime on U-series disequilibria, they did not attempt to account for the negative correlation between ^{226}Ra excess and ^{230}Th excess observed in MORB.

3.1. Model Formulation

To determine the effect of porous transport on U-series disequilibria in a system where melt is organized into high-porosity melt channels within a low-porosity background matrix, a simplified mass-conservative melt transport model is assumed (Fig. 2c). As the solid upwells and melts, the melt migrates upward through a porous matrix with a velocity that is driven by buoyancy and determined from the permeability, Darcy's law, and mass conservation. At a specified depth, high-porosity channels form, allowing rapid disequilibrium transport of some of the melt to the top of the melt column. The fraction of total melt flux that travels through the low-porosity interchannel region is a specified parameter (S); the remaining melt (1-s) travels through the high-porosity channel.

To quantify this model and calculate the effect of melt transport on radiogenic and stable trace element concentrations, equations of conservation of mass of melt and solid and of chemical species are required [see also Iwamori (1994) and Lundstrom (2000)]. For the following equations the parameters are defined in Table 1. For a one-dimensional steady state melting column, conservation of chemical species for a radio-

Table 1. Definition of parameters.

Symbol	Units	Meaning
ρ_f	kg m^{-3}	density of melt
ρ_s	kg m^{-3}	density of solid
$\Delta\rho$	kg m^{-3}	$\rho_f - \rho_s$
S		suction factor
λ	s^{-1}	decay constant
c^f		concentration of element in melt
c^s		concentration of element in solid
D		bulk solid/melt partition coefficient
K		mineral/melt partition coefficient
z	m	depth
Γ	kg s^{-1}	melting rate
ϕ		porosity
V_0	m s^{-1}	initial solid upwelling velocity
V	m s^{-1}	solid upwelling velocity during melting
v	m s^{-1}	melt velocity
w_{eff}	m s^{-1}	effective velocity of element in the melt
μ	Pa s	melt viscosity
F		degree of melting
k	m^2	permeability of solid matrix
g	m s^{-2}	gravitational constant
χ		fraction of high porosity conduits per unit length
b		permeability constant
d	m	grain size

genic element "i" in the low-porosity interchannel region ("1") and high-porosity channels ("2") gives

$$\frac{d}{dz}\left([\rho_f\phi_1 v_1 + \rho_s(1-\phi_1)D_i V]c^f_{i1}\right) = \lambda_{(i-1)}[\rho_f\phi_1 + \rho_s(1-\phi_1)D_i]c^f_{(i-1)1} - \lambda_i \cdot [\rho_f\phi_1 + \rho_s(1-\phi_1)D_i]c^f_{i1} - (1-S)\Gamma c^f_{i1}, \quad (1)$$

$$\frac{d}{dz}(\rho_f\phi_2 v_2 c^f_{i2}) = \lambda_{(i-1)}\rho_f\phi_2 c^f_{(i-1)2} - \lambda_i\rho_f\phi_2 c^f_{i2} + (1-S)\Gamma c^f_{i1}, \quad (2)$$

where v and V are the velocities of the melt and solid, ϕ is the porosity, ρ_f and ρ_s are the densities of the melt and solid, c is the concentration of an element, D is the bulk partition coefficient, λ is the decay constant, Γ is the melting rate, and S is a nondimensional scaling factor that specifies the fraction of the total melt flux that remains in region 1. Subscripts "$i-1$" and "i" refer to parent and daughter isotopes, respectively. Conservation of mass between solid and melt in region 1 requires

$$\frac{d}{dz}(\rho_f\phi_1 v_1) = S\Gamma, \quad (3)$$

$$\frac{d}{dz}(\rho_f\phi_2 v_2) = (1-S)\Gamma, \quad (4)$$

$$\frac{d}{dz}(\rho_s(1-\phi_1)V) = -\Gamma \quad (5)$$

which are solved to give relationships between melt and solid velocity

$$\rho_f\phi_1 v_1 = \rho_s V_0 F S, \quad (6)$$

$$\rho_f\phi_2 v_2 = \rho_s V_0 F(1-S), \quad (7)$$

$$\rho_s(1-\phi_1)V = \rho_s V_0(1-F). \quad (8)$$

Darcy flow is assumed in the porous matrix, giving

$$\phi(v - V) = \frac{k}{\mu}(1-\phi)\Delta\rho g \quad (9)$$

which can be approximated as

$$v = \frac{k\Delta\rho g}{\mu\phi} = \frac{d^2\phi^{n-1}\Delta\rho g}{\mu b}, \quad (10)$$

where $k = d^2\phi^n/b$ is the permeability. In this formulation, melting occurs only in the interchannel region (region 1), and the high-porosity channels (region 2) act only as pathways for disequilibrium transport of melt to the top of the melt column. These approximations are based on the assumption that the high-porosity channels are composed mainly of dunite and occupy a small percentage of the melting region ($\ll$10%). In addition, any residual clinopyroxene in the channels that remain after their formation is unlikely to significantly alter the ^{230}Th disequilibria, given the high porosities in the channel.

The porosity of the low-porosity region and the high-porosity channels is not only determined by the the relative proportions of the total melt flux required to travel through each region, but also by a weighting term χ which we introduce in order to approximate the horizontal extent of the high-porosity channels (e.g., Kelemen et al., 1997; Lundstrom, 2000). If the high-porosity channels transport the same fraction of the total melt flux over a smaller region, the porosity necessary to accommodate this increased flux must increase. Without this porosity "distribution parameter," the high-porosity channel would transport the same fraction of the total melt flux more slowly than a low-porosity region. To take into account the horizontal extent of high-porosity channels, we specify

Table 2. U, Th partition coefficients.

Reference	K_U	K_{Th}	K_U	K_{Th}
Lundstrom (2000)			1.5×10^{-2}	1.5×10^{-2}
Wood et al. (1999)			2.7×10^{-2}	2.9×10^{-2}
Salters and Longhi (1999)	2.8×10^{-2}	9.0×10^{-3}	5.0×10^{-3}	5.0×10^{-3}
Lundstrom et al. (1994)			1.0×10^{-2}	1.5×10^{-2}
Beattie (1993a, 1993b)	9.6×10^{-3}	1.5×10^{-3}	9.0×10^{-4}	1.3×10^{-3}
LaTourette and Burnette (1992)	1.5×10^{-2}	1.7×10^{-3}	4.5×10^{-3}	1.0×10^{-2}

$$\phi_1' = \frac{\phi_1}{(1-\chi)},\ \phi_2' = \frac{\phi_2}{\chi}, \tag{11}$$

and mass conservation requires

$$(1-\chi)v_1\phi_1'\rho_f + \chi v_2\phi_2'\rho_f = \rho_s V_0 F, \tag{12}$$

where $0 \leq \chi \leq 1$ is the proportion of the melting region occupied by the high-porosity channel Eqn. 12 states that the total flux of melt through the combined low- and high-porosity regions is conserved, and that the porosity in each region is a function of (χ) in that region.

Equations 1 and 2 apply to each radiogenic element in the decay chain, forming a coupled system of ordinary differential equations. An example of the behavior of Eqn. 1 can be obtained analytically for a stable element ($\lambda = 0$), with a solution (Iwamori, 1994)

$$\frac{c^f}{c_0} = \frac{1}{D}\left[\frac{D}{(S-D)F + D}\right]^{((1-D)/(S-D)}. \tag{13}$$

This equation reduces to fractional melting if $S = 0$ (100% efficiency of transfer of melt into high-porosity channels), or batch melting if $S = 1$ (all melt is retained in the low-porosity region). It is important to note that during fractional melting, incompatible elements are quickly depleted in the residual solid close to the solidus, whereas during batch melting (or equilibrium porous flow; Spiegelman and Elliott, 1993), the solid retains incompatible elements to shallow levels.

An important result of the conservation of mass equations is that each element has an "effective velocity" as it travels through the melt column, given by (e.g., Navon and Stolper, 1987; Spiegelman and Elliott, 1993):

$$w_{\text{eff}} = \frac{\rho_f\phi v + \rho_s(1-\phi)DV}{\rho_f\phi + \rho_s(1-\phi)D}. \tag{14}$$

Elements that are completely incompatible ($D = 0$) move with the melt velocity, while completely compatible elements ($D \Rightarrow \infty$) move with the solid velocity. This "chromatographic fractionation" alters the relative abundances of parent and daughter isotopes, because they have different residence times in the melt column.

Since the Darcy flux of melt is linearly related to the permeability, increasing the permeability decreases the porosity required to maintain a given melt flux. The permeability in our calculation used values of $n = 2$, $d = 4$ mm, $\mu = 10$ Pa s, and a constant of integration $b = 190$. These values are consistent with the theoretical results of Cheadle (private communication), von Bargen and Waff (1986) for an interconnected equilibrium melt network, the experimental results of Wark and Watson (1998) on H_2O–SiO_2, and the experiments of Viskupic et al. (2001) on olivine-melt. Faul (2001) argues that the permeability of partially molten peridotite changes dramatically in response to interconnection of melt filled "disks" at porosities greater than ~1%, and that the permeability of the mantle at porosities less than ~1% are orders of magnitude smaller than that predicted for isotropic permeability networks. This result is provocative, but Faul uses an average aspect ratio for each melt body, whereas in fact most melt—even in elongate bodies—resides in wide "pores" at triple grain junctions.

To generate ^{226}Ra and ^{230}Th excess from melting and melt transport, the parent element partition coefficient must be larger than that of the daughter. Table 2 gives mineral/melt partition coefficients (K's) for garnet and clinopyroxene cited in a number of references [experimentally determined except for Lundstrom (2000)], which are the two principle mineral phases that control solid/liquid partitioning of U, Th, and Ra. Partition coefficients for Ra have not been measured directly, but are inferred to be similar to Ba (1×10^{-4}) because of similar ionic radius (Wood et al., 1999). The variability in partition coefficients for U and Th may be due at least in part to the use of different mineral compositions in different experiments. However, it is clear that in garnet, U is more compatible than Th and this is often cited as the main reason for ^{230}Th excess in MORB. It is thought that in clinopyroxene, Th is either as compatible U or slightly more so, as is evident from the values listed in Table 1. Recent experiments by Salters and Longhi (1999) suggest that at high pressures in "fertile" bulk compositions (high Al, Na), U and Th have nearly identical partition coefficients in clinopyroxene. Wood et al. (1999) have argued that in high pressure fertile clinopyroxene (>1.5 GPa), U can be more compatible than Th, thus producing a ^{230}Th excess without the presence of garnet. Since melting probably begins at ~100 km (e.g., Hirth and Kohlstedt, 1996), well within the stability field for garnet lherzolite, we believe garnet does play a role in creating ^{230}Th excess, perhaps augmented by the effect of $K_U > K_{Th}$ in fertile clinopyroxene. In any case, it is generally agreed that ^{230}Th excess must be produced at the depth of initial melting, greater than 60 km, and that at shallower depths with more depleted clinopyroxene, $K_U \leq K_{Th}$. In our calculations we use $K_U = 2.8 \times 10^{-2}$ and $K_{Th} = 0.9 \times 10^{-2}$ for garnet (Salters and Longhi, 1999). For clinopyroxene we choose two end-member partition coefficients for Th and U; using values of $K_U = K_{Th} = 0.5 \times 10^{-2}$, which is in the range of values reported by Salters and Longhi (1999) and $K_U = K_{Th} = 3.0 \times 10^{-2}$ which is close to the values reported by Wood et al. (1999). These end-member partition coefficients for U and Th in clinopyroxene bracket the range of current experimental values and will be used in the following calculations.

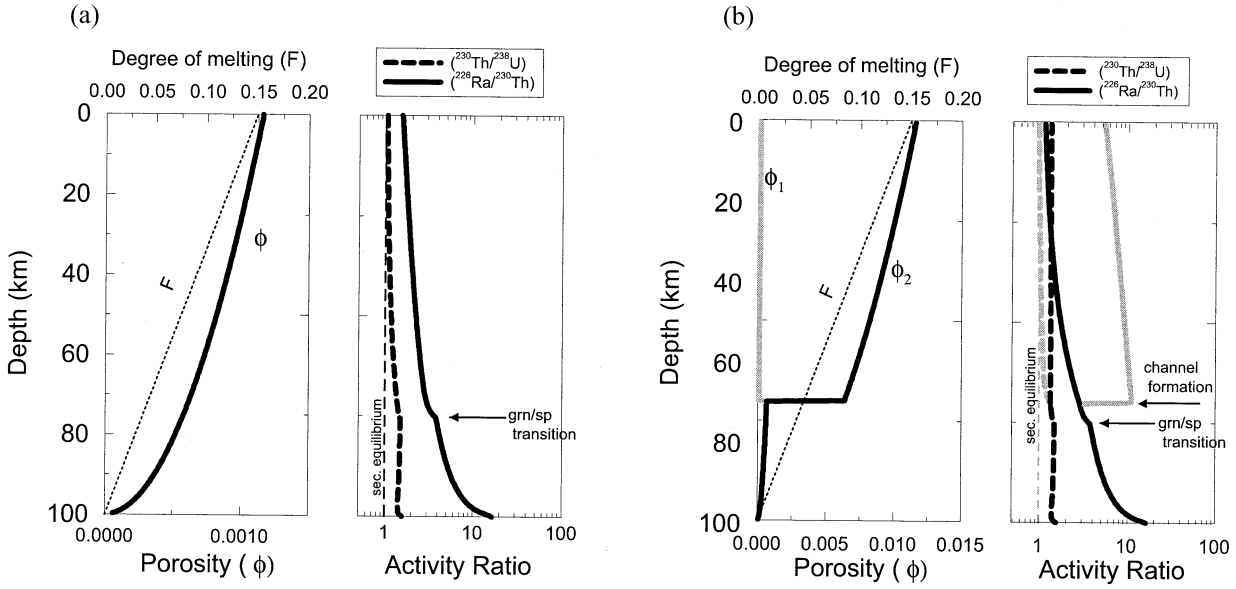

Fig. 3. Example of melt fraction, porosity, and calculated activity ratios along a melt column for (a) a single porous flow regime and (b) a porous flow regime in which high-porosity channels can form. In (a) all of the melt travels along the same pathway and is in equilibrium with the solid as it moves to the top of the melt column. The largest ^{226}Ra and ^{230}Th activity ratios are generated at the solidus and decrease as the melt travels to the top of the melt column, with the ^{230}Th activity ratios approaching secular equilibrium in the melt by the time the melt reaches the top of the melt column. In (b) a high-porosity channel is formed at a depth of 70 km, and the porosity along this channel is specified by ϕ_2, while the porosity in the surrounding low-porosity matrix is ϕ_1. The grey curves denote the activity ratios in the melt that travels along the low porosity (ϕ_1) pathway. In this example, which shows the basic behavior of the porous channel model, after formation of the channel 1% of the total melt flux is allowed to remain in the low-porosity region and 99% enters the high-porosity channel. The increase in ^{226}Ra excess and decrease in ^{230}Th excess in the melt after formation of the channel is due to lowered porosities in region "1" owing to the decreased melt flux and porosity. The ^{230}Th excess is only maintained in the high-porosity channel, while ^{226}Ra excess is only maintained in the low-porosity interchannel region. For this calculation $F = 0.15$, $\chi = 0.01$, and $V_0 = 1$ cm/yr are used. See text for further details.

Bulk distribution coefficients (D) are calculated for each element based on an assumed initial mineral mode for garnet pyrolite in the mantle which has ~13% clinopyroxene and ~8% garnet. The bulk D's are a function of the degree of melting, and at the garnet spinal transition (~75 km depth) garnet breaks down to spinal according to grn + ol $\Rightarrow$ sp + opx + cpx. The melting modes for garnet pyrolite are taken from Walter (1998) and for spinel pyrolite from Baker and Stolper (1994). Typically, for the degree of melting and the melting modes we assumed, at the top of the melt column there is ~5% clinopyroxene in the residual mantle.

3.2. Numerical Results

3.2.1. Diffuse porous transport

For a melt column in which $S = 1$, 100% of the melt transport is via diffuse, equilibrium porous flow, and all melt travels along the same path. An example of calculated ^{226}Ra and ^{230}Th activity ratios as a function of depth along a steady state melting column is shown in Figure 3a. In this calculation melting begins at 100 km depth, and the total degree of melting is 0.15. The porosity in the melt column increases in proportion to the melt flux at a given depth. Large ^{226}Ra and ^{230}Th excess are generated near the solidus, but decrease at shallow levels as the melt travels upwards through the melt column. Large excesses are generated near the solidus because the daughter elements are more incompatible than the parent elements ($D_{Ra} < D_{Th} < D_U$). As the melt moves towards the top of the melt column, reaction between solid and melt results in chromatographic fractionation of U, Th, and Ra. For the ^{226}Ra excess in Fig. 3a, even though Ra is more incompatible than Th throughout the melt column, the ^{226}Ra excess decreases because the large ^{226}Ra generated at the solidus cannot be maintained by the differential residence times of these elements in the melt column. For ^{230}Th, this effect is even more pronounced because $D_U = D_{Th}$ in the spinel stability field. The ^{230}Th excess generated at the solidus is therefore "unsupported" by the differential transport of Th and U during transport through the melt column, so that the ^{230}Th excess decays toward secular equilibrium. If $K_{Th} > K_U$ in clinopyroxene as the data in Table 2 suggest, the ^{230}Th excess generated at the solidus would be even harder to maintain because Th would spend longer in the melt column than U.

3.2.2. Diffuse and focused porous transport

An example of calculated activity ratios for a melting region in which high-porosity channels form in a low-porosity matrix is shown in Figure 3b, using the same D's as in Figure 3a, except that as soon as melt enters the high-porosity channel, the bulk D's are zero because the channels are assumed to be

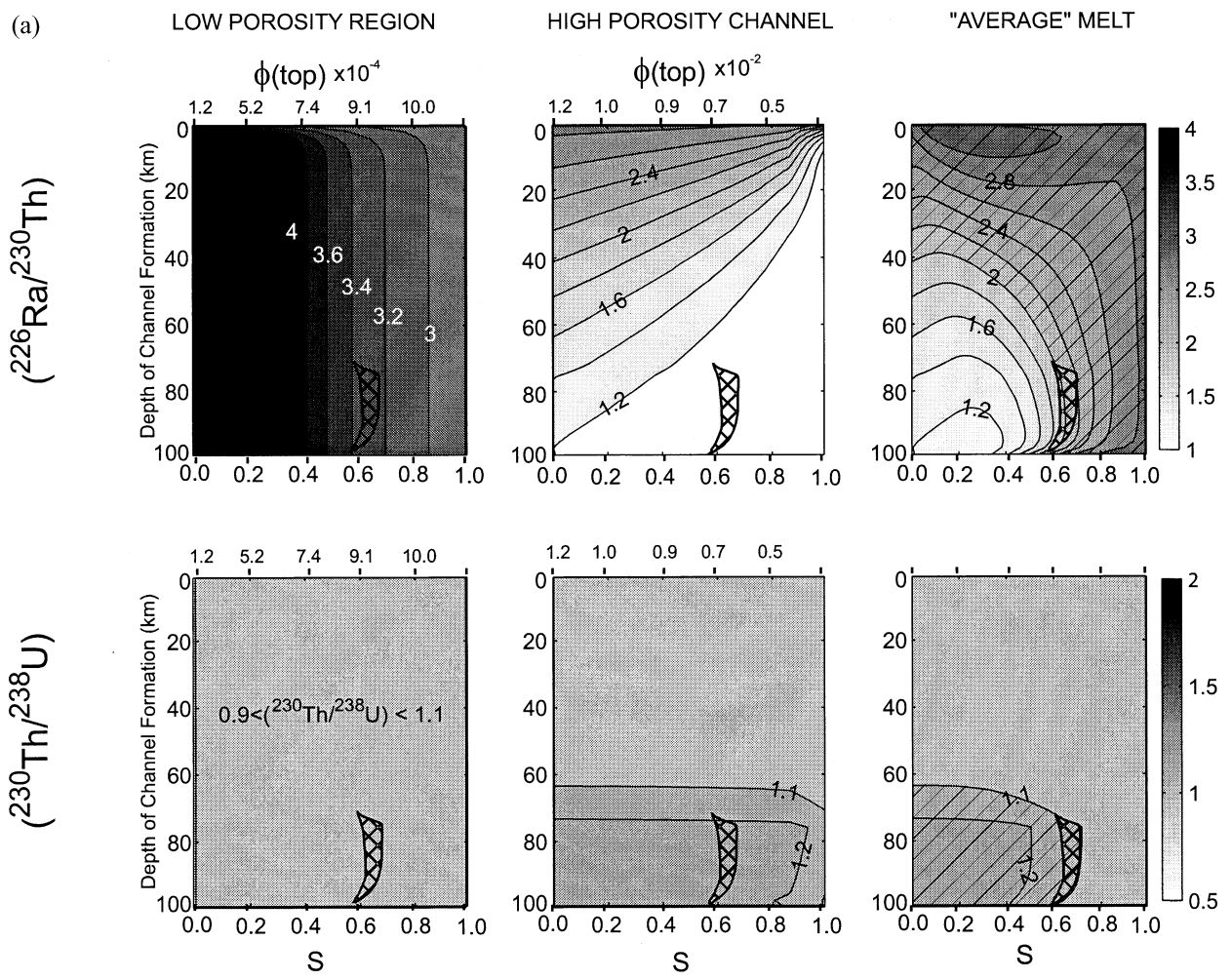

Fig. 4. Contours of calculated activity ratios at the top of the low-porosity region and the top of the high-porosity channels, and the average activity ratio of the melt as a function of the depth of channel formation and fraction of the total melt flux that remains in the low-porosity region *S*. In (a), K_{cpx} for U and Th are 3×10^{-2}, and in (b) 0.5×10^{-2}. For the average melt activity ratio, regions of the contour plot that are in the range of the average MORB data are marked with diagonal lines. The intersection of these regions for both ^{230}Th and ^{226}Ra activity ratios is marked by a "hatched" region which delineates the parameter range required to reproduce the average and end-member MORB data. In (b) there are no diagonal lines because the MORB data cannot be produced with the parameter range shown. In these calculations $F = 0.15$, $\chi = 0.01$, and $V_0 = 1$ cm/yr. See the text for further details.

mainly composed of dunite. In Figure 3b the channels form at a depth of 70 km in a melt column that extends to a depth of 100 km, with a total degree of melting of 0.15. After the channels form, 1% of the total melt flux (i.e., $S = 0.01$) is specified to remain in the low-porosity region, with the rest travelling through the high-porosity channels. The ^{230}Th excess decreases along the low-porosity pathway while the ^{226}Ra excess increases compared to Fig. 3a. Along the high-porosity pathway ^{226}Ra excess decreases while the ^{230}Th excess stays nearly constant. These results are encouraging and suggest that with this melt transport mode it is possible to generate the observed end-member radiogenic excesses and negative correlation indicated by the data.

Because the results of the calculations shown in Figure 3b are dependent on several parameters, including values chosen for S, V_0, F, χ, and the partition coefficients, K, we performed a series of calculations for different melt columns and then used the ^{226}Ra and ^{230}Th excess of melt arriving at the top of the low- and high-porosity pathways to determine the end-member and average (weighted by the flux) activity ratios. Figures 4a and 4b show contours of the ^{226}Ra and ^{230}Th activity ratios at the top of the low- and high-porosity regions as well as the mixed value (flux weighted average) as a function of depth of channel formation and fraction of total melt flux (S) remaining in the low-porosity region for two different sets of partition coefficients. In Figure 4a K_{cpx} for U and Th are 3×10^{-2}, and in Figure 4b K_{cpx} for U and Th are 0.5×10^{-2}. In these results, the depth of channel formation varies from 0–100 km (i.e., from the shallow mantle to the solidus), and the fraction of total melt flux remaining in the low-porosity region varies from $S = 0$–1 (i.e., 0%–100% of the melt flux remains in the low-porosity region). Other parameter values used in these calculations are listed in the figure caption.

In the "average melt" panels in Figure 4a, contours of activ-

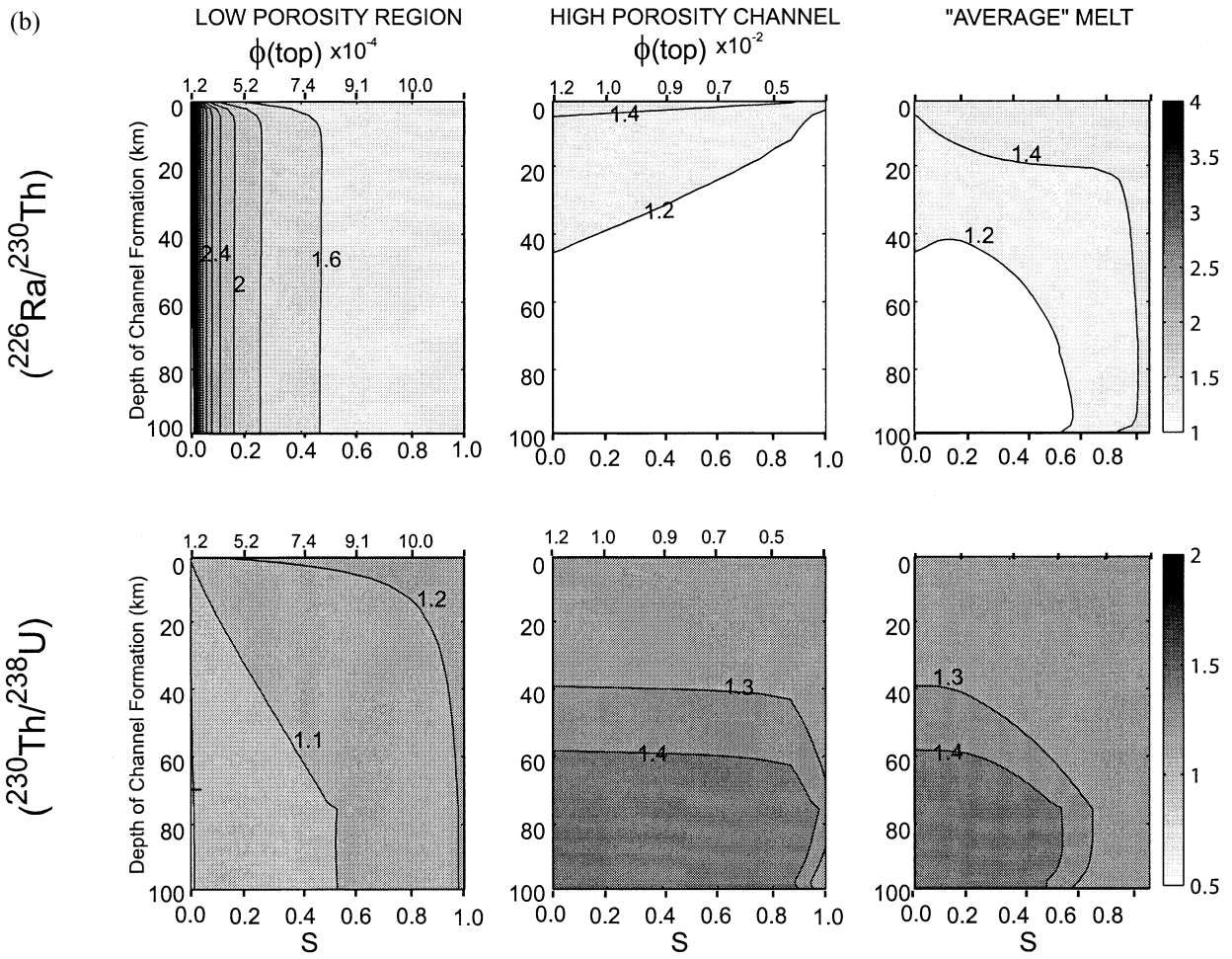

Fig. 4. continued

ity ratios that fall within the observed range of MORB from 9–10 °N on the East Pacific Rise (~2–3 for ^{226}Ra excess and ~1.1–1.2 for ^{230}Th excess) are highlighted with diagonal lines. The overlap of the highlighted regions for the ^{226}Ra and ^{230}Th excesses delineates the range of parameter values that can reproduce the U-series data and are shown with a hatched pattern. The hatched pattern is also shown in the panels for the low-porosity region and high-porosity channels, giving the end-member activity ratios from each region. It is clear from these results that by using the larger K_{cpx} values for U and Th IFig. 4a), it is possible to produce the observed range in U-series excess if the high-porosity channels are formed deep (>60 km) and if ~60% of the total melt flux passes through the low-porosity region (i.e., $S = 0.6$). With the smaller K_{cpx} values for U and Th (Fig. 4b) it is not possible to generate the observed range in U-series excesses. Note that from the contours in Figure 4b, at small melt fluxes through the low-porosity region (~$S = 0.01$) it is possible to reproduce high ^{226}Ra excesses, but these low concentration melts do not contribute significantly to the mixed melt composition at the top of the melt column, as can be seen in the "average" melt activity ratio.

Comparison of calculated activity ratios to the U-series data are shown in Figure 5. For these results we used K_{cpx} values for U and Th of 0.5, and 3.0×10^{-2}. The effect of changes in the total degree of melting, mantle upwelling rates, and volume fraction of high-porosity conduits are shown, but for these calculations the percentage of the total melt flux in the low-porosity region is held constant at 60% ($S = 0.6$). We specified different depths of channel formation for models with different clinopyroxene partition coefficients in order to generate a ^{230}Th excess in the range of the data. These values are 70 km, and 50 km for the 3.0 and 0.5 m $\times 10^{-2}$ K values used for clinopyroxene. Larger K values for U and Th in clinopyroxene require deeper channel formation in order to maintain ^{230}Th excesses in the spinel stability field. It is clear from the results in Figure 5 that to reproduce the U-series disequilibria data, the clinopyroxene partition coefficients of 3×10^{-2} are needed. The data are best fit if the upwelling rate is <5 cm/yr and the maximum degree of melting is <0.15. With the clinopyroxene partition coefficients used in Figure 5b (0.5×10^{-2}) it is not possible to fit the U-series data for reasonable parameter values.

Decreasing the percentage of the total melt flux in the low-porosity region can allow the observed negative correlation in the U-series data to be generated with smaller U and Th partition coefficients for clinopyroxene. However, the concentrations of U, Th and Ra in the low-porosity, high ^{226}Ra excess end-member are negligible. Figure 6 shows this for both high and low clinopyroxene K values used in Figure 5 and using

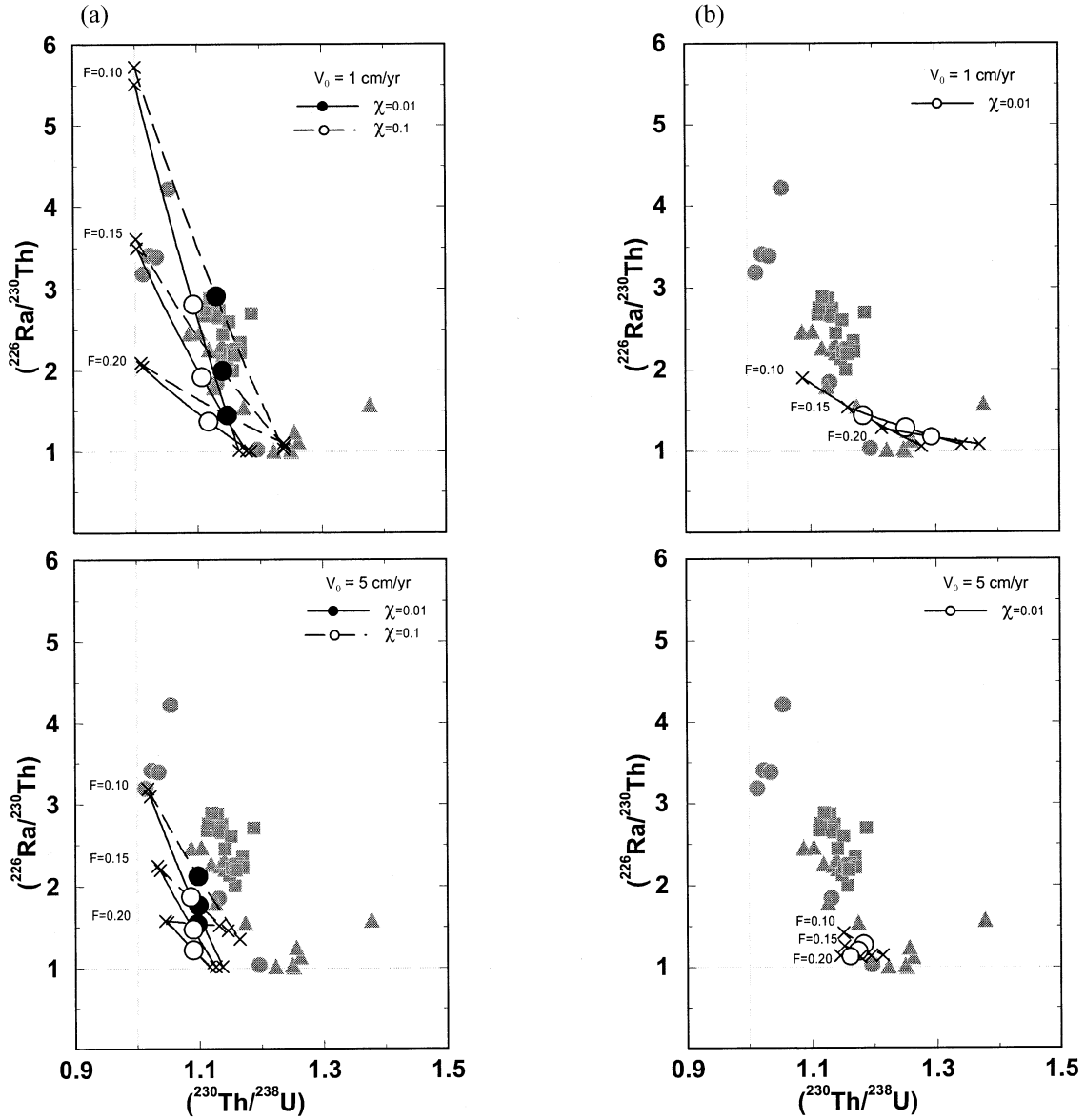

Fig. 5. Comparison of calculated activity ratios from the low- and high-porosity regions to the U-series data for a number of different parameter values that highlight the essential behavior of the high-porosity channel transport model. The flux weighted average activity ratio from the calculations are shown as a circle along the mixing lines. In (a) K_{cpx} for U and Th are 3×10^{-2}, and in (b) 0.5×10^{-2}. The bottom plots show the effect of increased solid upwelling velocities (V_0) on activity ratios but using the same parameters as in the top plots. The value of S used in these calculations is 0.6, meaning that 60% of the total melt flux remains in the interchannel region.

values of S ranging from 0.99 to 0.01. Also listed are end-member concentrations of U, Th, and Ra in the melt for the calculations shown in Figure 6a. It is clear that as the percentage of the total melt flux through the low-porosity region decreases, the ^{226}Ra excess increases because of reduced porosities. Nevertheless, the average mixed melt composition approaches the composition of the high-porosity channel end-member (high ^{230}Th and low ^{226}Ra excess) due to the negligible concentration of ^{226}Ra is in the low-porosity end-member. It is therefore not possible to reproduce the U-series data unless more than about half ($S \geq 0.5$) of the melt flux stays in the low-porosity region.

Sims et al. (2002, Figs. 9a–f, and Fig. 11) show that ^{226}Ra excess is negatively correlated with La/Yb and Th/U and positively correlated with Sm/Nd in data from 9–10 °N on the East Pacific Rise. ^{230}Th excesses show the opposite correlations with these chemical indices. We calculated the variation of ^{230}Th and ^{226}Ra excess as a function of $\alpha_{Sm/Nd}$, La/Yb, and Th/U (Fig. 7). For these calculations we used rare earth element partition coefficients compiled by Kelemen et al. (1993) and an initial depleted mantle source. In addition we employed a two-stage melting function, that assumed .25% melting in the garnet stability field (depth interval from 100 to 75 km) and 14.75% melting in the spinal stability field (<75 km) but kept

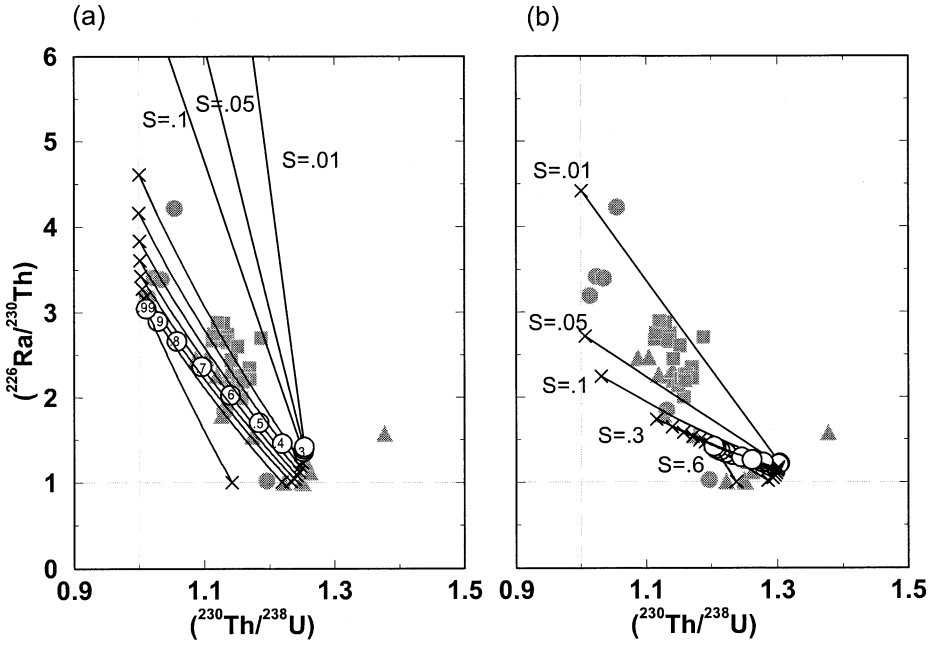

	Region 1			Region 2		
S	[238U]	[230Th]	[226Ra]	[238U]	[230Th]	[226Ra]
0.01	1.10E-11	1.10E-11	1.70E-10	5.83	7.31	10.4
0.1	1.80E-03	1.80E-03	1.30E-02	5.8	7.3	10
0.3	0.46	0.46	2.11	5.9	7.3	9.1
0.6	2.9	2.9	10.5	5.9	7.3	7.9
0.9	5.7	5.8	18.2	5.9	7.2	7.3

Fig. 6. Comparison of calculated activity ratios from the low- and high-porosity regions to the U-series data, as in Fig. 5, but with values of S ranging from 0.99−0.01 (i.e., 99% to 1% of the total melt flux remains in the low-porosity region). For these results $F = 0.15$, $\chi = 0.01$, and $V_0 = 1$ cm/yr. K_{cpx} for U and Th are 3×10^{-2} in (a) and 0.5×10^{-2} in (b). Shown in the table are end-member source normalized concentrations of ^{238}U, ^{230}Th, and ^{226}Ra in the melt at the top of the low and high porosity regions (regions 1 and 2, respectively) corresponding to the results in (a).

the total degree of melting constant at 15%. The two-stage melting function maintains a larger fractionation between different incompatible elements before formation of the channels, but has little effect on the ^{230}Th excesses generated at the base of the melt column because porosities remain significantly smaller than the bulk partition coefficient of U. Melt from the top of the low- and high-porosity regions were mixed (weighted by the flux) to form an average melt composition. Results are shown in Figure 7 for different proportions of the total melt flux passing through the low-porosity region. The correlations and average compositions show good agreement with the data reported in Sims et al. (2002) if ~60% of the total melt flux passes through the low-porosity region.

Comparison of calculated and observed (abyssal peridotite) trace element concentrations in the residual solid mantle are shown in Figure 8. In the calculations, the residual mantle corresponds to the top of the low-porosity region and values of S are shown ranging from 0.01-0.6 (light solid lines; the dark solid line corresponds to the initial solid concentration). A value of $S = 0.6$ (i.e., 60% of the total melt flux remains in the low-porosity region), which can reproduce the U-series disequilibria and stable trace element data, does not produce as large a depletion in incompatible elements as is observed in most of the abyssal peridotite data (Johnson et al., 1990). To assess the effect of increased efficiency of melt transfer to the high porosity channels in the shallow mantle, we show results where the melt flux through the low porosity interchannel region decreases to zero over the last 15 km of the melt column (dashed lines). This has the effect of increasing the degree of depletion in the residual solid, and allows a better fit of the calculated trace element concentrations in the residual mantle with the abyssal peridotite data.

4. DISCUSSION

It is clear from the results that only a narrow range of parameters can reproduce the observed U-series disequilibria via a melt transport model in which high-porosity channels form in a low-porosity matrix. The range of parameters is reasonable given our understanding of melting beneath a mid-ocean ridge and experimental work on solid–liquid partitioning of incompatible elements. However, it is worth considering how much the constraints from modeling can be relaxed to accomodate larger degrees of melting, faster upwelling rates, and smaller partition coefficients for U and Th in clinopyroxene. It is relatively straightforward to account for the ^{230}Th excess because of its longer half-life; the only requirement being that it must be isolated from the matrix at some depth

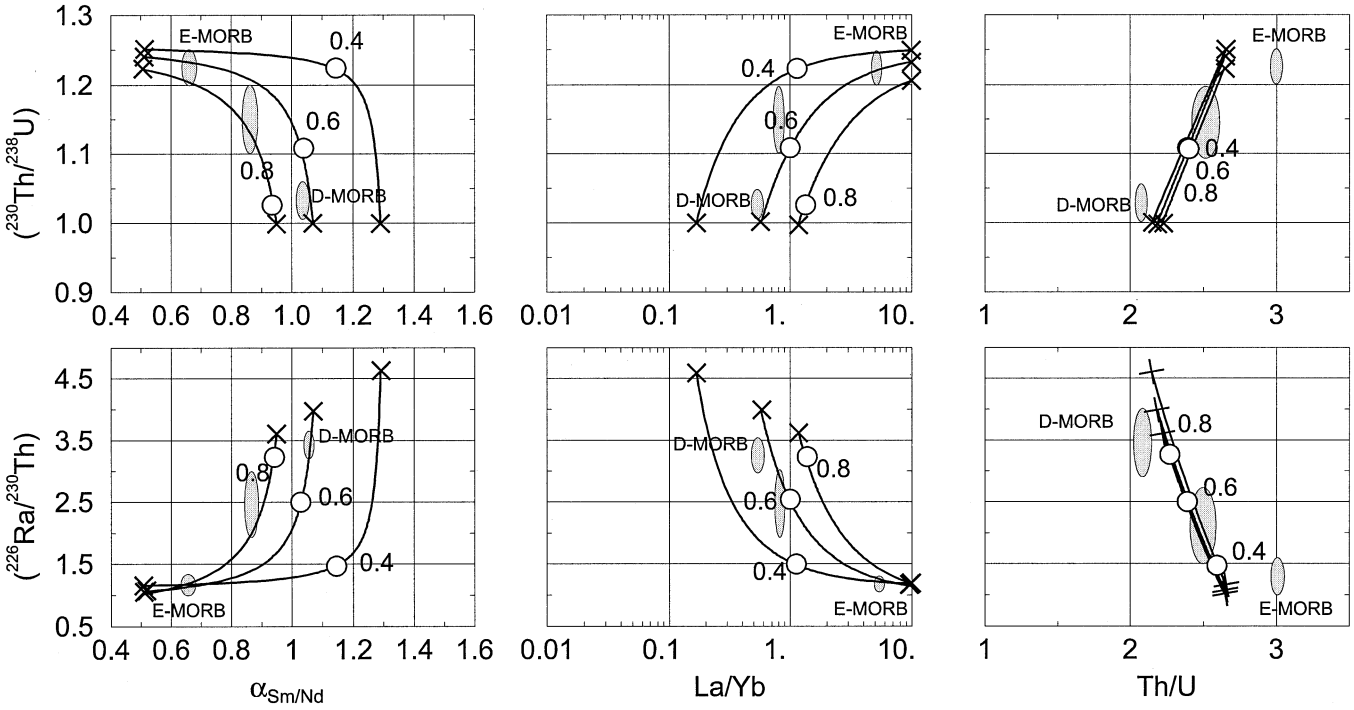

Fig. 7. Calculated trace element concentrations in melts that travel via diffuse low-porosity flow and high-porosity channels. Mixing lines are shown for three different values of S 0.8, 0.6, and 0.4. End-member melt compositions from the low porosity region are shown as white triangles, from the high porosity region as white circles, and the average melt is shown as a black square. Also shown are ellipses which define the data fields for $\alpha_{Sm/Nd}$, La/Yb, and Th/U (see Sims et al., 2002). These calculations used a two-stage melting function, with a lower melt productivity at the bottom of the melt column and a higher melt productivity near the top. See text for details.

(depending on the U and Th partition coefficients) as the melt migrates to the surface. In contrast, to generate the ^{226}Ra excess requires porosities to be either small, or the partition coefficient of Th to be large. This is not the place to speculate on mineral/melt partitioning of Th, or on source and melt modes in the subridge mantle, but clearly the experimental data are not yet internally consistent. One way to reduce the porosity further, and still maintain significant melt flux through the low-porosity region, is by increasing the permeability. The permeability used in this study was constrained by theoretical and experimental data, whereas in many models of melt flow in the mantle, values have been adjusted to fit other constraints. We think our

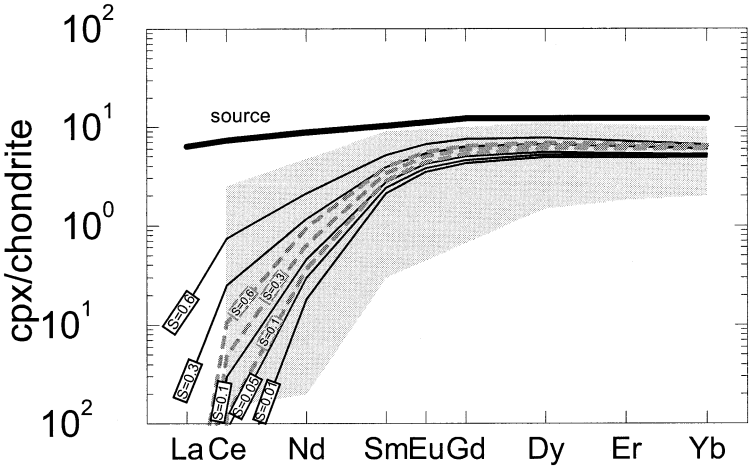

Fig. 8. Residual solid trace element concentrations in the low-porosity region as a result of values of S of 0.01, 0.05, 0.10, 0.30, 0.60 compared to the abyssal peridotite data of Johnson et al. (1990)—shown as the shaded region. Dashed lines show the residual solid trace element concentrations at the top of the melt column for initial values of S of 0.6, 0.3, and 0.1 if S decreases to 0.01 in the last 15 km of the melt column.

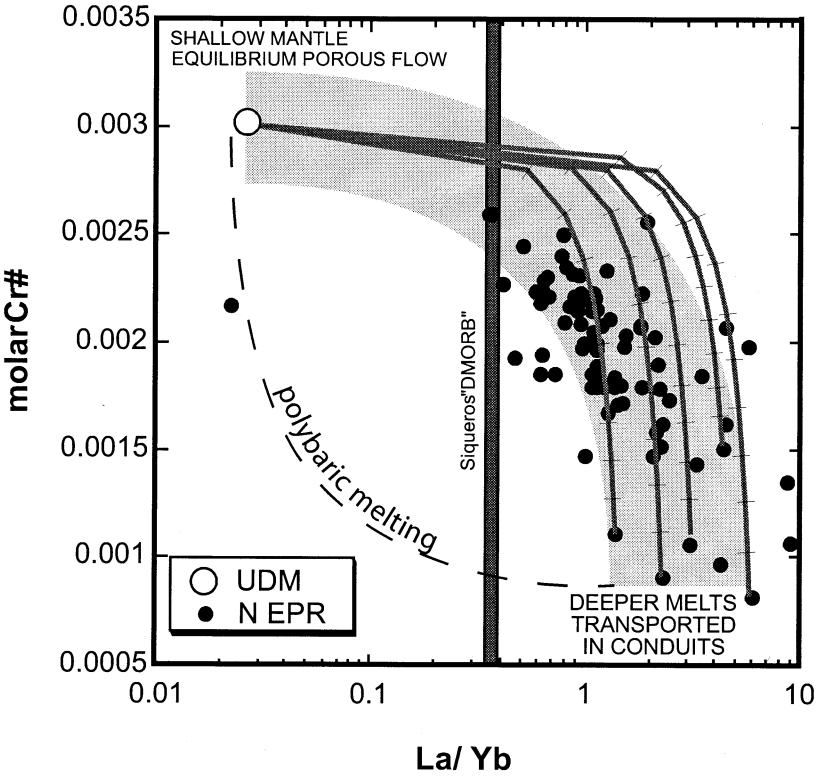

Fig. 9. Composition of MORB glasses from the East Pacific Rise compiled from the RIDGE Petrological Database. For Cr# (= Cr/(Cr + Al)) versus log(La/Yb) the data show a concave downward, rather than concave upward, trend, suggesting the mixing of melts from deep in the melt column with those melts that have equilibrated at shallower levels. Calculated mixing curves with 10% increments are also shown. Mid-Atlantic Ridge ultradepleted melt composition is from Sobolev and Shimizu (1993). [Concentrations (ppm) in UDM are $[Cr_2O_3] = 0.07$, $[Al_2O_3] = 15.5$, [La] = 0.015, [Yb] = 0.57, and representative end-member MORB are $[Cr_2O_3] = 0.0178$, $[Al_2O_3] = 18.1$, [La] = 30.04, [Yb] = 2.26.]

approach is preferable, but remind the reader that the permeability remains poorly known.

The conclusion that large amounts of melt (more than half of all primitive MORB) must travel via porous equilibrium flow through the mantle, while the rest of the melt must travel in disequilibrium with the mantle via high-porosity unreactive channels is consistent with observations from both MORB chemistry and from residual depleted peridotite data. The composition of mid-ocean ridge basalts (MORBs) themselves suggest ubiquitous mixing of liquids from relatively deep in the melting column with melts that have remained in equilibrium with the mantle until shallow levels. For example, Sims et al., (1999, Fig. 3) investigated trends of ^{230}Th excess vs. the degree of melting inferred from Sm/Nd ratios and Nd isotopes. They found that Hawaiian data fit calculated fractional and dynamic melting trends, whereas MORB could be interpreted as a mixture of high- and low-degree melts, with intermediate-degree melts omitted. Our interpretation of these data is that, in fact, the less-depleted MORB end-member is melt that has travelled within high-porosity channels, without reaction with the shallow mantle, whereas the more-depleted MORB end-member is formed by melts that have equilibrated via porous flow with the shallow mantle.

Similarly, Kelemen et al. (1997) pointed out that spinels in primitive MORB generally have Cr/Al ratios as high as in the most depleted abyssal peridotites, but REE patterns indicative of equilibrium with much less depleted peridotites. As for the data discussed in the preceding paragraph, this could record mixing of disequilibrium, "channel melts" with melts that have equilibrated with the shallow mantle in approximately equal proportions. In this context, some "ultra-depleted melt" (UDM) compositions found in Atlantic, olivine-hosted melt inclusions (e.g., Sobolev and Shimizu, 1993) could be liquids that equilibrated with shallowest mantle peridotite, so that they approached equilibrium with the most depleted mantle residues (melt/rock ratio $< 10–3$), rather than being high-degree, low-pressure, near-fractional melts.

To investigate this possibility more thoroughly, we used data for glasses in lava samples from the East Pacific Rise, from the RIDGE Petrological Database (www.ldeo.columbia.edu/RidgePetDB), to compare variation in compatible versus incompatible elements. The data were filtered to include only lavas with molar Mg# [Mg/(Mg + Fe) > 0.6] to mitigate or remove the effects of crystal fractionation. Success of this procedure was verified by the fact that, within these high Mg# MORB data, there is no correlation of Cr# with Mg#. The data (and those from Atlantic MORB—not shown) form trends on plots of Cr# versus log(La/Yb) (Fig. 9) which are concave downward, rather than concave upward. Concave upward trends are predicted for a series of liquids formed by different degrees of mantle melting because at increasing degrees of melting the La/Yb ratio decreases. In contrast, concave down-

ward to linear trends on these diagrams are consistent with mixing of relatively high- and low-degree melts, without incorporation of intermediate-degree melts. This is because the high degree melts have higher Cr concentrations, but low La and Yb concentrations, thus changing the La/Yb ratio of the deep melts very little until large fractions of high degree melt are added. In Figure 9, calculated mixing lines with mixing increments of 10% are shown using the UDP shallow, high degree melt composition and several different melt compositions for the deep "low-degree melt" end-member. The data fall near the 50–60% proportion of the shallow mantle component in the mixing calculation. The steeper slope in the mixing calculations compared to the trend in the data is a result of our assumption of the UDP end-member for the mixing calculation—a less depleted shallow melt would decrease the curvature of the mixing line. From these results, it is clear that some compositional variation in Pacific and Atlantic laws is consistent with a process in which primitive MORB is formed by mixing of two distinct liquids, one relatively enriched liquid that last equilibrated with the mantle at deeper levels within the melting region, and another, depleted liquid which equilibrated with the mantle at shallower depths.

The highly light REE depleted nature of residual mantle peridotites in ophiolites and in dredge and drill core samples from the mid-ocean ridges ("abyssal peridotites") has been interpreted to mean that there is little or no interaction between these residual peridotites and migrating melt (e.g., Johnson et al., 1990; Johnson and Dick, 1992; Dick and Natland, 1996). Instead, these samples were viewed as residues of a near-fractional melting process in which melt is removed by porous flow. Implicit in this view is the inference that no melt migrating from elsewhere in the melting region passes through these residual rocks. When it is phrased in this way, such a hypothesis seems physically implausible, and indeed Iwamori (1994), Kelemen et al. (1997), Niu (1997) argued that most residual peridotites do, in fact, record the effects of small amounts of reaction with migrating melt. Nonetheless, the "typical," depleted, residual mantle peridotites from ophiolites and mid-ocean ridges do not record a process in which about half of MORB reacts with shallow mantle peridotites.

Thus, our model, which requires about 60% of the total melt flux to react with the "residual" peridotite at any given level above the base of the channels, seems to be discrepant with the abyssal peridotite data. However, this is not a particularly strong constraint. Both abyssal peridotite suites and ophiolite mantle peridotite suites also include less depleted samples (e.g., abyssal peridotites, Johnson et al., 1990, Figure 6; Dick and Kelemen, 1991; Seyler and Bonatti, 1997; Oman ophiolite, shallowest sample OMB-43 of Kelemen et al., 1995, Figure 3; Bay of Islands ophiolite, Suhr and Cawood, 1993; Suhr, 1999; Red Hills Peridotite, Sano, 1992; Trinity ophiolite, Kelemen et al., 1992, Figure 4; Kelemen et al., 1997, Fig. 4). Tellingly, these less depleted samples have higher light REE concentrations in clinopyroxene compared to "typical," highly depleted abyssal peridotites as do our model results for shallow peridotite at the top of the low-porosity melting zone (Fig. 8).

Further, the minimum depth to which equilibrium porous flow continues in the shallow mantle is not well constrained in our models. There is no requirement in our model that melt must remain in equilibrium with the mantle up to the Moho. In addition to the refractory trace element characteristics of the shallow mantle peridotite, one observation that suggests equilibrium porous flow does not continue to the Moho is that liquids parental to MORB are not saturated in orthopyroxene (opx) at Moho pressures (e.g., O'Hara, 1965; Stolper, 1980; Elthon and Scarfe, 1980), whereas opx is a major constituent of mantle peridotites dredged and drilled from mid-ocean ridges and at ophiolites. Thus, at the shallowest levels in the mantle, the volume of melt that remains in equilibrium with the mantle does not constitute a large proportion of MORB.

Therefore, if there is significant reactive porous flow of melt through the residual mantle as our results suggest, there must be some additional process that decreases this proportion in the upper ~30 km of melt transport through the shallow mantle. For example, it is possible that the efficiency of transfer of melt to the high-porosity channels is not simply a "step" function, as we have assumed. Instead, the efficiency of melt transfer from residual peridotite into channels increases in response to the continued growth of the channels via a positive feedback reactive infiltration instability (see Spiegelman et al., 2001). The effect of such a process would be to further deplete the residual shallow mantle in trace elements, as is observed in abyssal peridotites (see Fig. 8). At shallow depths melt from the low-porosity regions, which have large ^{226}Ra excesses and no ^{230}Th excesses, are transferred to the high-porosity channels and transported in disequilibrium with the shallowest mantle to the Moho. The efficiency of mixing in the channel would dictate the degree to which the activity ratios were "homogenized," thus accounting for the relatively scarce high ^{226}Ra and low ^{230}Th excess samples found in MORB. Also, additional channels may form at shallower levels in the mantle, thus excluding the high ^{230}Th melts and providing an isolated conduit for transport of high ^{226}Ra melts through the shallowest mantle.

Despite evidence from abyssal peridotites and MORB chemistry that the shallowest level melt transport in the mantle is via some disequilibrium transport mechanism, it should be kept in mind that there do exist "impregnated" peridotites in ophiolite mantle and abyssal peridotite suites worldwide. The presence of "impregnated" peridotites in the shallow mantle section of ophiolites (e.g., Ceuleneer and Rabinowicz, 1992, and references therein), and in dredge and drill core samples from mid-ocean ridges (e.g., Dick, 1989; Seyler and Bonatti, 1997; Dick and Natland, 1996), indicates that melt/rock reaction is a common phenomenon in the shallow mantle beneath some sections of oceanic spreading ridges.

5. CONCLUSIONS

A negatively correlated array of ^{230}Th and ^{226}Ra activity ratios from young MORB samples indicate that ^{226}Ra and ^{230}Th excess are produced independently. Dynamic (near fractional) melting, in which melt is isolated from the residual solid and rapidly transported to the surface, cannot explain this negative correlation. Melt transport via equilibrium porous flow, in which high-porosity channels form in a background low-porosity matrix, can produce a negative correlation of ^{226}Ra and ^{230}Th activity ratios. To fit the observed data, ~60% of the total melt flux in the mantle must travel via equilibrium porous flow. Given theoretical and experimental constraints on mantle permeability, the range of parameters required to fit the

U-series data are narrow, requiring a total degree of melting ≤ 0.15, solid mantle upwelling rates ≤ 5 cm/yr, and clinopyroxene partition coefficients for U and Th of about $3\ \mathrm{m} \times 10^{-2}$. Calculation of the degree of trace element fractionation in the melt and residual solid for this parameter range give trends that are consistent with MORB, and fall within the range of abyssal peridotite data. These results support the conclusion that equilibrium porous flow occurs extensively in the mantle beneath spreading ridges. Equilibration of MORB with the shallow mantle is not required to continue up to the base of the crust in order to reproduce the U-series and trace element data in our models. Instead, we propose that enhanced transfer of melt from reactive, residual peridotite into high-porosity dunite channels occurs in the shallowest portions of the mantle, at pressures $<\sim 8$ kbar.

Acknowledgments—The authors would like to thank Greg Hirth and Karen Hanghoj for helpful comments and discussions. This paper was greatly improved by extensive reviews provided by Craig Lundstrom and Marc Spiegelman. This work was supported by a NSERC-WHOI postdoctoral fellowship to Jull, OCE-9730967 to Sims, EAR-0087706 to Jull and Kelemen, and OCE-9819666 to Kelemen. This paper is WHOI contribution 10716.

Associate editor: F. A. Frey

REFERENCES

Aharonov E., Spiegelman M., and Kelemen P. (1997) Three-dimensional flow and reaction in porous media; implications for the Earth's mantle and sedimentary basins. *J. Geophys. Res.* **102,** 14821–14833.

Aharonov E., Whitehead J. A., Kelemen P. B., and Spiegelman M. (1995) Channeling instability of upwelling melt in the mantle. *J. Geophys. Res.* **100,** 20433–20450.

Baker M. B. and Stolper E. M. (1994) Determining the composition of high-pressure mantle melts using diamond aggregates. *Geochim. Cosmochim. Acta* **58,** 2811–2827.

Batiza R. and Niu Y. (1992) Petrology and magma chamber processes at the East Pacific Rise approximately 9 degrees 30'N. *J. Geophys. Res.* **97,** 6779–6797.

Beattie P. (1993a) On the occurrence of apparent non-Henry's law behaviour in experimental partitioning studies. *Geochim. Cosmochim. Acta* **57,** 47–55.

Beattie P., Drake M., Jones J., Leeman W., Longhi J., McKay G., Nielsen R., Palme H., Shaw D., Takahashi E., and Watson B. (1993b) Terminology for trace-element partitioning. *Geochim. Cosmochim. Acta* **57,** 1605–1606.

Ceuleneer G. and Rabinowicz M. (1992) Mantle flow and melt migration beneath oceanic ridges: models derived from observations in ophiolites. *Geophys. Mon.* **71,** 123–154.

Connolly J. A. and Podladchikov Y. Y. (1998) Compaction-driven fluid flow in viscoelastic rock. *Geodinamica Acta* **11,** 55–84.

Dick H. J. B. (1989) Abyssal peridotites very slow spreading ridges and ocean ridge magmatism (ed. A. D. Saunders and M. J. Norry) Magmatism in the ocean basins. *Geol. Soc. Spec. Pub.* **42,** 71–105.

Dick H. J. B. and Kelemen P. B. (1991) Chromian spinel as a petrogenetic indicator of magma genesis in shallow mantle rocks, AGU–MSA 1991 spring meeting. *EOS. Trans. Am. Geophys. Union* **72,** 142.

Dick H. J. B. and Natland J. H. (1996) Late-stage melt evolution and transport in the shallow mantle beneath the East Pacific Rise, Proceedings of the Ocean Drilling Program. *Scientific Results* **147,** 103–134.

Elthon D. and Scarfe C. M. (1980) High-pressure phase equilibria of a high-magnesia basalt; implications for the origin of mid-ocean ridge basalts, *Geological Society of America, 93rd annual meeting, Abstracts with Programs—Geological Society of America*, Vol. 12, p. 421.

Faul U. (2001) Melt retention and segregation beneath mid-ocean ridges. *Nature* **410,** 920–923.

Goldstein S. J., Murrell M. T., and Janecky D. R. (1989) Th and U isotopic systematics of basalts from the Juan de Fuca and Gorda Ridges by mass spectrometry. *Earth Planet. Sci. Lett.* **96,** 134–146.

Hall C. and Parmentier E. M. (1998) Melt migration beneath oceanic spreading centers with realistic mantle rheologies; effects of melt-retention viscosity reduction, AGU 1998 spring meeting. *Eos, Trans. Am. Geophys. Union* **79,** 232.

Hirth G. and Kohlstedt D. L. (1996) Water in the oceanic upper mantle; implications for rheology, melt extraction and the evolution of the lithosphere. *Earth Planet. Sci. Lett.* **144,** 93–108.

Iwamori H. (1994) ^{238}U–^{230}Th–^{226}Ra and ^{235}U–^{231}Pa disequilibria produced by mantle melting with porous and channel flows. *Earth Planet. Sci. Lett.* **125,** 1–16.

Johnson K. T. M., Dick H. J. B., and Shimizu N. (1990) Melting in the oceanic upper mantle: an ion microprobe study of diopsides in abyssal peridotites. *J. Geophys. Res.* **95,** 2661–2678.

Johnson K. T. M. and Dick H. (1992) Open system melting and temporal and spatial variation of peridotite and basalt at the Atlantis II fracture zone. *J. Geophys. Res.* **97,** 9219–9241.

Kelemen P. B. (1990) Reaction between ultramafic rock and fractionating basaltic magma; I, Phase relations, the origin of calc-alkaline magma series, and the formation of discordant dunite. *J. Petrol.* **31,** 51–98.

Kelemen P. B., Dick H. J. B., and Quick J. E. (1992) Formation of harzburgite by pervasive melt/rock reaction in the upper mantle. *Nature* **358,** 635–641.

Kelemen P. B., Shimizu N., and Dunn T. (1993) Relative depletion of niobium in some arc magmas and the continental crust: partitioning of K, Nb, La and Ce during melt/rock reaction in the upper mantle. *Earth Planet Sci. Lett.* **120,** 111–134.

Kelemen P. B. and Dick H. J. B. (1995) Focused melt flow and localized deformation in the upper mantle; juxtaposition of replacive dunite and ductile shear zones in the Josephine Peridotite, SW Oregon. *J. Geophys. Res.* **100,** 423–438.

Kelemen P. B., Shimizu N., and Salters V. J. M. (1995) Extraction of mid-ocean-ridge basalt from the upwelling mantle by focused flow of melt in dunite channels. *Nature* **375,** 747–753.

Kelemen P. B., Hirth G., Shimizu N., Spiegelman M., and Dick H. J. B. (1997) A review of melt migration processes in the adiabatically upwelling mantle beneath oceanic spreading ridges. *Philos. Trans. R. Soc. London* **355,** 1–35.

LaTourrette T. Z. and Burnett D. S. (1992) Experimental determination of U and Th partitioning between clinopyroxene and natural and synthetic basaltic liquid. *Earth Planet. Sci. Lett.* **110,** 227–244.

Lundstrom C. C., Shaw H. F., Ryerson F. J., Phinney D. L., Gill J. B., and Williams Q. (1994) Compositional controls on the partitioning of U, Th, Ba, Pb, Sr and Zr between clinopyroxene and haplobasaltic melts; implications for uranium series disequilibria in basalts. *Earth Planet. Sci. Lett.* **128,** 407–423.

Lundstrom C. (2000) Models of U-series disequilibria generation in MORB; the effects of two scales of melt porosity. *Phys. Earth Planet. Int.* **121,** 189–204.

Lundstrom C. C., Gill J., Williams Q., and Perfit M. R. (1995) Mantle melting and Basalt extraction by equilibrium porous flow. *Science* **270,** 1958–1961.

Lundstrom C. C., Williams Q., and Gill J. B. (1998) Investigating solid mantle upwelling rates beneath mid-ocean ridges using U-series disequilibria; 1, A global approach. *Earth Planet. Sci. Lett.* **157,** 151–165.

Lundstrom C. C., Sampson D. E., Perfit M. R., Gill J., and Williams Q. (1999) Insights into mid-ocean ridge basalt petrogenesis; U-series disequilibria from the Siqueiros Transform, Lamont Seamounts, and East Pacific Rise. *J. Geophys. Res.* **104,** 13035–13048.

McKenzie D. (1985) ^{230}Th-^{238}U disequilibrium and the melting processes beneath ridge axes. *Earth Planet. Sci. Lett.* **72,** 149–157.

McKenzie D. (2000) Constraints on melt generation and transport from U-series activity ratios. *Chem. Geol.* **162,** 81–94.

Navon O. and Stolper E. (1987) Geochemical consequences of melt percolation; the upper mantle as a chromatographic column. *J. Geol.* **95,** 285–307.

Nicolas A. (1989) *Structures of Ophiolites and Dynamics of Oceanic Lithosphere*. Kluwer Academic.

Nicolas A. (1990) Melt extraction from mantle peridotites: hydrofracturing and porous flow, with consequences for oceanic ridge activity. In: *Magma Transport and Storage* (ed. M. P. Ryan), pp. 159–1784. Wiley.

Niu Y. (1997) Mantle melting and melt extraction processes beneath spreading ridges: evidence from abyssal peridotites. *J. Petrol.* **38,** 1047–1074.

O'Hara M. J. (1965) Primary magmas and the origin of basalts. *Scott. J. Geol.* **1,** 19–40.

O'Hara M. J. (1968) Are any ocean floor basalts primary? *Nature* **220,** 683–686.

Reinitz I. and Turekian K. K. (1989) $^{230}Th/^{238}U$ and $^{226}Ra/^{230}Th$ fractionation in young basaltic glasses from the East Pacific rise. *Earth Planet. Sci. Lett.* **94,** 199–207.

Richardson C. N. (1998) Melt flow in a variable viscosity matrix. *Geophys. Res. Lett.* **25,** 1099–1102.

Rubin K. H. and MacDougall J. D. (1990) Dating of neovolcanic MORB using ($^{226}Ra/^{230}Th$) disequilibrium. *Earth Planet. Sci. Lett.* **101,** 313–321.

Salters V. J. M. and Longhi J. (1999) Trace element partitioning during the initial stages of melting beneath mid-ocean ridges. *Earth Planet. Sci. Lett.* **166,** 15–30.

Sano S. (1992) Petrogenesis of the Red Hills peridotite in the Dun Mountain ophiolite belt, 29th International Geological Congress **29,** 136.

Seyler M. and Bonatti E. (1997) Regional-scale melt-rock interaction in lherzolitic mantle in the Romanche fracture zone (Atlantic Ocean). *Earth Planet. Sci. Lett.* **146,** 273–287.

Sims K. W., Goldstein S. J., Blicher-Toft J., Perfit M. R., Kelemen P., Fornari D. J., Michael P., Murrell M. T., Hart S. R., DePaolo D. J., Layne G., and Jull M. (2002) U-series analyses of young axial lavas from 9–10°N East Pacific Rise: Constraints on magma transport and storage times beneath the ridge axis. *Geochim. Cosmochim. Acta* in press.

Sims K. W. W., DePaolo D. J., Murrell M. T., Baldridge W. S., Goldstein S., Clague D., and Jull M. (1999) Porosity of the melting zone and variations in the solid mantle upwelling rate beneath Hawaii: Inferences from ^{238}U–^{230}Th–^{226}Ra and ^{235}U–^{231}Pa disequilibria. *Geochim. Cosmochim. Acta* **63,** 4119–4138.

Sleep N. H. (1988) Tapping of melt by veins and dikes. *J. Geophys. Res.* **93,** 10255–10272.

Sobolev A. V. and Shimizu N. (1993) Ultra-depleted primary melt included in an olivine from the Mid-Atlantic Ridge. *Nature* **363,** 151–154.

Spiegelman M. and Elliott T. (1993) Consequences of melt transport for uranium series disequilibrium in young lavas. *Earth Planet. Sci. Lett.* **118,** 1–20.

Spiegelman M., Kelemen P., and Aharonov E. (2001) Causes and consequences of flow organisation during melt transport: the reaction infiltration instability. *J. Geophys. Res.* **106,** 2061–2077.

Spiegelman M. and Reynolds J. (2000) Geochemistry in motion: Combined theoretical and observational evidence for convergent melt flow beneath the East Pacific Rise. *Nature* **402,** 282–285.

Stevenson D. J. (1989) Spontaneous small-scale melt segregation in partial melts undergoing deformation. *Geophys. Res. Lett.* **16,** 1067–1070.

Stolper E. (1980) "Predictions of mineral assemblages in planetary interiors." In Igneous Processes and Remote Sensing (ed. P. R. Criswell and R. B. Merrill). *Proc. L. Planet. Sci. Conf.* **1,** 235–250.

Suhr G. (1999) Melt migration under oceanic ridges; inferences from reactive transport modelling of upper mantle hosted dunites. *J. Petrol.* **40,** 575–599.

Suhr G. and Cawood P. A. (1993) Structural history of ophiolite obduction, Bay of Islands, Newfoundland. *Geol. Soc. Am. Bull.* **105,** 399–410.

Viskupic K., Renner J., Hirth G. Evans B. (2001) Melt segregation from partially molten peridotites. Presented at *AGU*.

Volpe A. M. and Goldstein S. J. (1993) ^{226}Ra–^{230}Th disequilibrium in axial and off-axis mid-Ocean ridge basalts. *Geochim. Cosmochim. Acta* **57,** 1233–1242.

von Bargen N. and Waff H. S. (1986) Permeabilities, interfacial areas, and curvatures of partially molten systems; results of numerical computations of equilibrium microstructures. *J. Geophys. Res.* **91,** 9261–9276.

Walter M. (1998) Melting of garnet peridotite and the origin of komatiite and depleted lithosphere. *J. Petrol.* **39,** 29–60.

Wark D. A. and Watson E. B. (1998) Grain-scale permeabilities of texturally equilibrated, monomineralic rocks. *Earth Planet. Sci. Lett.* **164,** 591–605.

Wood B. J., Blundy J. D., and Robinson J. A. C. (1999) The role of clinopyroxene in generating U-series disequilibrium during mantle melting. *Geochim. Cosmochim. Acta* **63,** 1613–1620.